Draft version May 18, 2017
Typeset using LaTeX **twocolumn** style in AASTeX61

A CATALOG OF 3MM POINT SOURCES IN THE SGR B2 CLOUD: SIGNS OF EXTENDED STAR FORMATION IN A CMZ CLOUD

Adam Ginsburg[1,2]

[1] *Jansky fellow of the National Radio Astronomy Observatory, Socorro, NM 87801 USA*

[2] *European Southern Observatory, Karl-Schwarzschild-Straße 2, D-85748 Garching bei München, Germany*

ABSTRACT

We report ALMA observations at 3 mm of the extended Sgr B2 cloud. We detected 237 sources in the Sgr B2 clouds, the majority of which have extents smaller than 5000 AU. These sources are predominantly protostars or centrally condensed prestellar cores. The spatial distribution of these sources demonstrates that Sgr B2 is experiencing a highly extended star formation event, not just an isolated 'starburst' within the protocluster regions M, N, and S. While all protostars reside in regions of high column density, not all regions of high column density possess a high density of protostars.

Corresponding author: Adam Ginsburg
aginsbur@nrao.edu; adam.g.ginsburg@gmail.com

1. INTRODUCTION

The Central Molecular Zone (CMZ) of our Galaxy appears to be overall deficient in star formation relative to the gas mass it contains (Longmore et al. 2013; Kauffmann et al. 2016a,b; Barnes et al. 2016, 2017). This deficiency suggests that star formation laws, i.e., the empirical relations between the star formation rate and gas density, are not universal. The gas conditions in the Galactic center provide a powerful lever-arm in a few parameters (e.g., pressure, temperature, velocity dispersion Ginsburg et al. 2016; Immer et al. 2016; Shetty et al. 2012; Henshaw et al. 2016) to assess the influence of environmental effects on star formation.

The observations that have demonstrated the star formation deficiency compare bulk tracers of star formation to $\gtrsim 0.1$ pc resolution gas observations (Barnes et al. 2017, e.g.). More recently, high-resolution observations of selected clouds in the CMZ have revealed very few star-forming cores even when examined at high resolution and sensitivity (Rathborne et al. 2015; Kauffmann et al. 2016a,b). The only sites with obvious signs of ongoing star formation along the CMZ dust ridge are the Sgr B2 N, M, and S protoclusters (Schmiedeke et al. 2016) and, at a much lower level, Clouds C, D, and E (Ginsburg et al. 2015, Walker et al, in prep; Barnes et al, in prep). These regions contain a handful of high-mass cores detected with ALMA, but only a small number of protostars.

We report the first observations of extended, ongoing star formation in a Galactic center cloud *not* isolated to a centralized protocluster dust clump. We observed a $\sim 15 \times 15$ pc section of the Sgr B2 cloud and identified star formation along the entire molecular dust ridge known as Sgr B2 Deep South (DS). These observations allow us to perform the first star-counting based determination of the star formation rate within the molecular gas of the CMZ.

We describe the observations in Section 2. In this paper, we focus on the continuum sources, which we identify in Section 3.1. We classify the sources in Section 4.1.

2. OBSERVATION AND DATA REDUCTION

Data were acquired as part of ALMA project 2013.1.00269.S. Observations were taken with the 12m Total Power array, the ALMA 7m array, and in two configurations with the ALMA 12m array. The setup included the maximum allowed number of channels, 30720, across 4 spectral windows in a single polarization; the single-polarization mode was adopted to support moderate spectral resolution across the broad bandwidth.

The ALMA QA2 calibrated measurement sets were combined to make a single high-resolution, high-dynamic range data set. We imaged the continuum jointly across all four bands, and found that the central regions surrounding Sgr B2 M were severely affected by artifacts that could not be cleaned out. We therefore ran 3 iterations of phase-only self-calibration and two iterations of amplitude + phase self-calibration, the latter using multi-scale multi-frequency synthesis with two Taylor terms, to yield a substantially improved image. The total dynamic range, measured as the peak brightness in Sgr B2 to the RMS noise in a signal-free region of the combined 7m+12m image, is 18000 (noise ~ 0.09 mJy/beam), while the dynamic range within one primary beam ($\sim 0.5'$) of Sgr B2M is only 5300 (noise ~ 0.3 mJy/beam). Because of the dynamic range limitations, and an empirical determination that clean did not converge if allowed to go too deep, we cleaned to a threshold of 0.5 mJy/beam across the image. We performed this same process for both the longest-baseline data only (resolution $\sim 0.5''$, largest angular scale theoretically $15''$ [the shortest baseline] but more practically $\sim 7''$ [the 5th percentile baseline length]) and the merged 7m + two 12m configuration data. The merged data are more useful for studying extended structures but have lower dynamic range, while the long-baseline-only data are excellent for extracting and analyzing pointlike or compact sources.

We also produced cubes of all of the spectral lines. These were lightly cleaned with a maximum of 2000 iterations of cleaning to a threshold of 100 mJy/beam. No self-calibration was applied. Before continuum subtraction, dynamic range related artifacts similar to those in the continuum images were present, but these structures are identical across frequencies, and were therefore removable in the image domain. We use median-subtracted cubes for the majority of our analysis, noting that the only location in which an error on the continuum $> 5\%$ is expected is the Sgr B2 North core (Sanchez-Monge et al. 2017).

2.1. *Column Density Maps*

We use archival data from SCUBA, SHARC, and Herschel to create column density maps. We combined the SHARC and SCUBA data with Herschel SPIRE 350 and 500 μm images (Molinari et al. 2010), respectively. The data combination is discussed in detail in Appendix A.

The SHARC data were reported in Bally et al. (2010) and have a nominal resolution of $9''$ at 350 μm, however, at this resolution, the SHARC data display a much higher surface brightness than the Herschel data on a similar scale. A resolution of $11.5''$ gives a better surface brightness match and is consistent with the measured scale of Sgr B2 N in the image. This calibration difference is likely to have been a combination of blurring by pointing errors, surface imperfections, and the gridding process, and by flux calibration errors. In any case, the Herschel data provide the most trustworthy absolute calibration scale.

The SCUBA 450 μm data were reported in Pierce-Price et al. (2000) and Di Francesco et al. (2008) with a resolution of 8″. We found that the SCUBA data had a flux scale significantly discrepant from the Herschel data, even accounting for the central wavelength difference. We had to scale the SCUBA data up by a factor ≈ 3.0 to make the data agree with the Herschel images on the angular scales they are both hypothetically sensitive to. While such a large flux calibration error seems implausible, the measured FWHM is approximately 14″, which means the beam area is $\approx 3\times$ larger than the theoretical size. We attempted to fit several other isolated sources in the large SCUBA map, and the smallest FWHM we measured was ≈ 10.5 arcsec. Between the larger beam area, flux calibration errors (quoted at 20% in Pierce-Price et al. 2000), and the dust emissivity correction (35-50% for $\beta = 3 - 4$), this large flux scaling factor is actually plausible.

To determine the column density, we adopted a few independent approaches. First, we use the Herschel data to perform SED fits to each pixel (Battersby et al, in prep). We performed these fits at 25″ resolution, excluding the 500 μm channel. To obtain higher resolution column density maps, we used the combined Herschel-SHARC and Herschel-SCUBA maps assuming optically thin dust using both a constant temperature and the temperature measured with Herschel at 25″ resolution interpolated onto the higher-resolution SCUBA and SHARC grids. Because of the interpolation or fixed temperature assumptions, the column maps are not very accurate and should not be used for systematic statistical analysis of the column distribution.

3. ANALYSIS

3.1. *Continuum Source Identification*

We selected continuum point sources as candidate cores or protostars by eye. An automated selection is not viable across the majority of the field because there are many extended H II regions that dominate the overall map emission. A future automated selection algorithm may work if images at comparable resolution at other frequencies become available; the H II-region sources could then be excluded. Additionally, however, there are substantial imaging artifacts produced by the extremely bright emission sources in Sgr B2 M ($S_{3mm,max} > 0.8$ Jy) and Sgr B2 N ($S_{3mm,max} > 0.3$ Jy) that make automated source identification particularly challenging in the most source-dense regions.

Because the noise varies significantly across the map, a uniform selection criterion is not possible. We therefore include two levels of source identification, 'high confidence' sources, which are selected conservatively in regions of low-background, and 'low-confidence' sources that are somewhat lower signal-to-noise and are often in regions with higher background. Both of these selection criteria are significantly more conservative than a local $5 - \sigma$ threshold.

We measure the local noise for each source by taking the median absolute deviation in an annulus 0.5 to 1.5 ″ around the source center. All but 7 sources have signal-to-local-noise ratios $S/N > 7$. These sources are all in regions of particularly high background or source density and therefore have overestimated local noise.

Our selection criteria result in a reliable but potentially incomplete catalog.

For a subset of the sources, primarily the brightest, we measured the spectral index α. We relied on CASA's α and $\sigma(\alpha)$ maps to obtain these measurements, including only those with $|\alpha| > 5\sigma(\alpha)$ or $\sigma(\alpha) < 0.1$. Several of the brightest sources did not have significant measurements of α because they are in the immediate neighborhood of Sgr B2 M or N and therefore have significantly higher background and noise, preventing a clean measurement.

4. RESULTS

We detected 237 compact continuum sources. Their flux distribution is shown in Figure 1. The distribution of their measured spectral indices α is shown in Figure 2.

4.1. *Source Classification*

For the majority of the detected sources, we have only a continuum detection at 3 mm. No lines are detected peaking toward most of the sources, especially the faint ones. A subset have detections at other bands and can be classified based on previous literature work, especially those associated with H II regions detected at 0.7 and 1.3 cm (Gaume et al. 1995; Mehringer et al. 1995; de Pree et al. 1996; Pree et al. 2015). In this section, we employ various means to classify the sample of new sources.

We first note some key properties of dust at 3 mm. At 8.4 kpc, a 1 mJy source corresponds to an optically thin dust mass of $M(40\mathrm{K}) = 18\ M_\odot$ or $M(20\mathrm{K}) = 38\ M_\odot$ assuming a dust opacity index $\beta = 1.75$ ($\alpha = 3.75$ on the Rayleigh-Jeans tail) to extrapolate the Ossenkopf

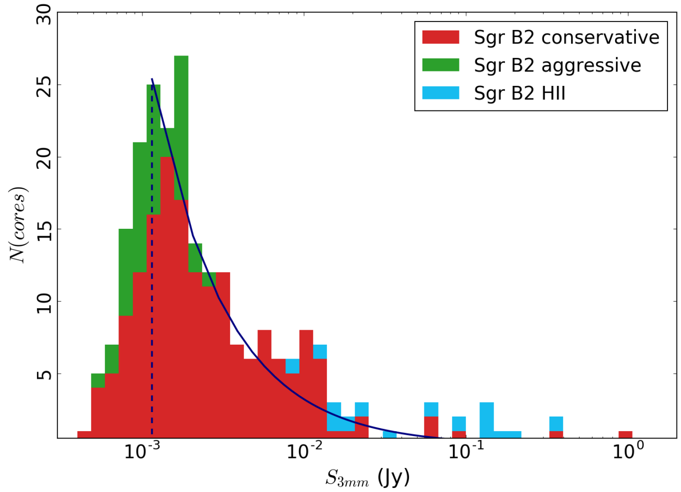

Figure 1. A histogram of the peak flux density of the observed sources excluding known H II regions with a powerlaw fit shown. The fitted powerlaw is an excellent fit to the data, but is far shallower than the IMF slope, with $\alpha = 1.94 \pm 0.07$. The two brightest regions are Sgr B2M f1 and Sgr B2N K2, which may be dominated by free-free emission but likely also contain a large dust mass.

& Henning (1994) opacity to $\kappa_{3mm} = 0.0018$ cm^2 g^{-1}. Our dust-only 5-σ sensitivity limit at 40 K therefore ranges from $M > 7\ M_\odot$ (0.5 mJy) to $M > 45\ M_\odot$ (2.5 mJy) across the map. If we were to assume that these are all cold, dusty sources, as is typically (and reasonably) assumed for local clouds, they would be extremely massive and dense, with the lowest measurable density being $n(40\mathrm{K}) > 3 \times 10^6$ cm^{-3} (corresponding to $7\ M_\odot$ in a $0.5''$ radius sphere). Such extreme objects are possible, but since we have detected >100 of these sources, we evaluate other possibilities.

4.1.1. *Alternative 1: The sources are externally ionized gas blobs*

One possibility is that these sources are not dusty at all, nor pre- or protostellar, but are instead the brightest compact clumps surrounding H II regions. They would then be analogous to the heads of cometary clouds, externally ionized globules ("EGGs"), or proplyds, and their observed emission would give no clue to their nature because the light source is extrinsic.

The majority of the detected sources have size <4000 AU, i.e., they are unresolved. By contrast, the free-floating EGGs so far observed have sizes 10,000-20,000 AU (Sahai et al. 2012a,b), so they would be resolved in our observations. Toward the brightest frEGG in Cygnus X, Sahai et al. (2012b) measured a peak intensity $S_{8.5GHz} \approx 1.5$ mJy/beam in a $\approx 3''$ beam. Cygnus X is 6× closer that the Galactic center, so their beam size is the same physical scale as ours. If the free-free emission is thin, the brightness in our data would be $S_{95GHz} = (95/8.5)^{-0.1} S_{8.5GHz} = 0.79 S_{8.5GHz} \approx 1.2$ mJy/beam. These frEGGs would be detectable in our data. Comparison to radio observations at a comparable resolution will be needed to rule out the externally ionized globule hypothesis for resolved regions.

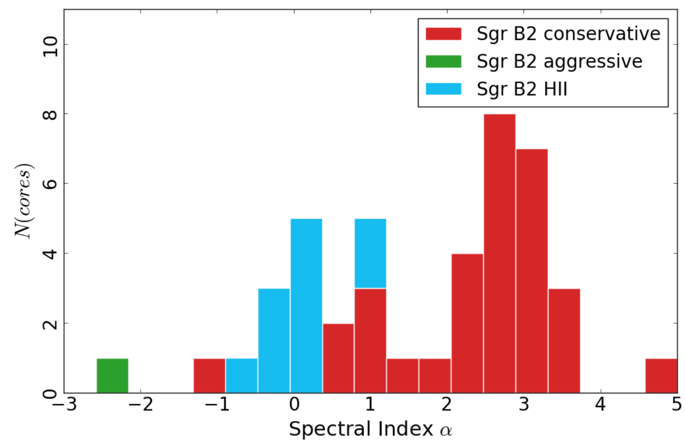

Figure 2. A histogram of the spectral index α for those sources with a statistically significant measurement. The H II regions cluster around $\alpha = 0$, as expected for optically thin free-free emission, while the unclassified sources cluster around $\alpha = 3$, which is weakly consistent with dust emission. There are two particularly notable outliers: the source with a highly negative spectral index, Source 167, has a statistically significant measurement but is in a region of particularly high extended and diffuse background, so the measurement may not be reliable. The other unidentified source with $\alpha \sim -1$ is Source 80, which is very close to the H II region Sgr B2 S, but is not detected in the de Pree et al. (1996) 1.3 cm data; it may be an H II region or it may be contaminated by the nearby H II region.

If the detected sources were either EGGs or cometary clouds, we would expect them to be located within H II regions. Many of the sources are near H II regions, as seen in Figure 3. However, they are nearly all associated with a ridge of HC_3N emission (Figure 4). If they are deeply embedded within the molecular material, they cannot be externally ionized. The current data do not provide enough information on the geometry of the clouds to rule out the possibility that the point sources are just illuminated cloud edges, but the fact that the ionized gas is brightest adjacent to, rather than on top of, the HC_3N suggests that the HC_3N traces a full molecular cloud rather than a thin PDR-like layer.

A final point against the externally ionized hypothesis is the observed spectral indices shown in Figure 2. We measured spectral indices for 43 sources, of which 23 have $\alpha > 2$. These sources are inconsistent with free-free emission and are at least reasonably consistent with dust emission. Of the 20 that are consistent with free-free emission, 11 are known H II regions, hinting that our sample is dominated by dusty objects, not externally ionized objects.

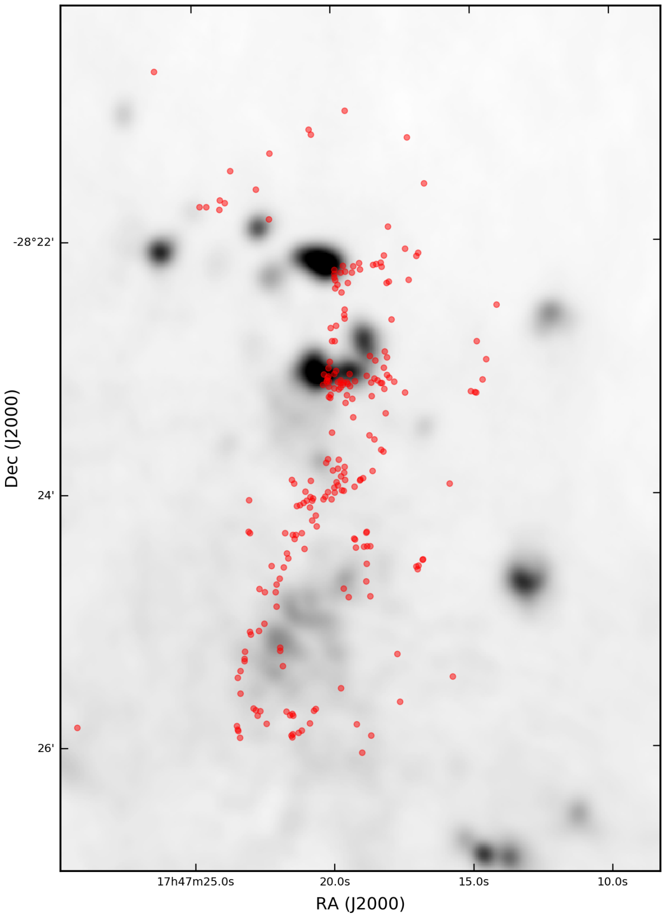

Figure 3. The location of the detected continuum sources (red points) overlaid on a 20 cm continuum VLA map highlighting the diffuse free-free (or possibly synchrotron) emission in the region (Yusef-Zadeh et al. 2004).

4.1.2. *Alternative 2: The sources are* H II *regions produced by interloper ionizing stars*

If there is a large population of older, but still ionizing, stars, they could ignite H II regions when they fly through molecular material. See 4.1.3 for calculations of stationary H II region properties. The main problem with this scenario is the spatial distribution of the observed sources. While most of the continuum sources are associated with dense gas and dust ridges, not all of the high-column molecular gas regions have such sources in them (i.e., the left and right sides of the image in Figure 4, where molecular material is seen with no associated millimeter sources). If there is a free-floating population

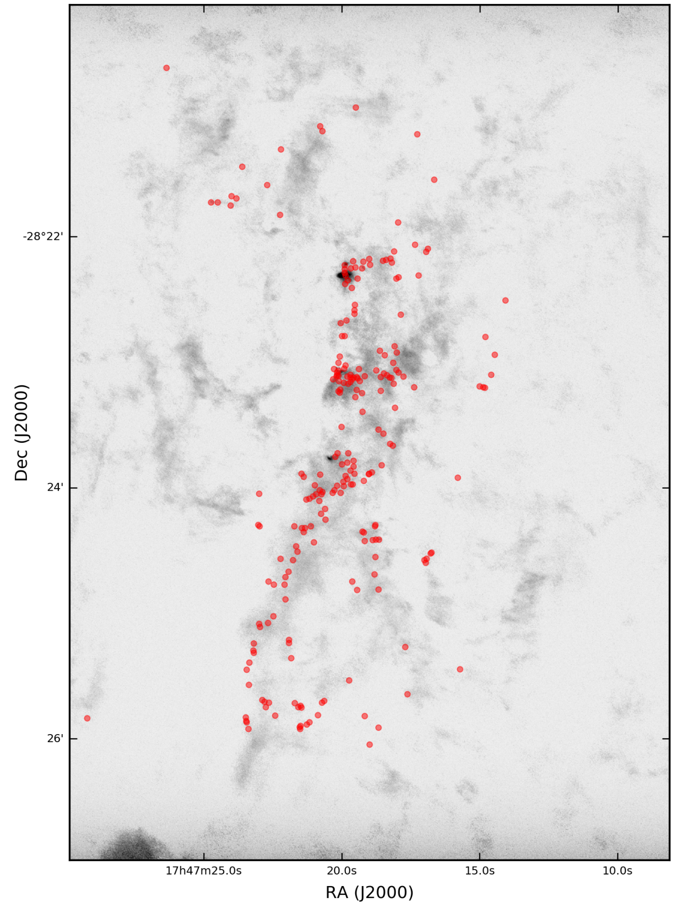

Figure 4. The location of the detected continuum sources (red points) overlaid on a map of the HC_3N peak intensity. HC_3N traces moderate-density molecular gas.

of OB stars responsible for the 3 mm point source population, their distribution should match that of the gas. Also, there is no such population of sources seen outside of the dense gas in the infrared (TODO: Who has done infrared studies of Sgr B2? You can infer what I have stated 'by inspection' of 2MASS, but it would be more straightforward to quote someone else), which again we should expect if there is a uniformly distributed population. Finally, the spectral indices discussed above (Figure 2) suggest the previously-unidentified sources are dust emission sources, not free-free sources.

4.1.3. *Alternative 3: The sources are* H II *regions produced by recently-formed OB stars*

For an unresolved spherically symmetric H II region ($R = 4000$ AU), the expected flux density is $S_{95\mathrm{GHz}} = 4.7$ mJy for a $Q_{lyc} = 10^{47}$ s^{-1} source (assuming $T_e = 7000$ K), and that value scales linearly with Q_{lyc} as long as the source is optically thin. Rearranging Condon &

Ransom (2007) equations 4.60 and 4.61:

$$\begin{aligned} S_\nu(Q_{lyc}) &= 4.67\left[1-\exp\left(c_* T_* \nu_* EM_*\right)\right] \\ \nu_* &= \left(\frac{\nu}{\mathrm{GHz}}\right)^{-2.1} \\ T_* &= \left(\frac{T_e}{10^4\mathrm{K}}\right)^{-1.35} \\ c_* &= -3.28\times10^{-7} \\ EM_* &= \frac{3Q_{lyc}}{4\pi R^2 \alpha_b} \end{aligned} \tag{1}$$

where $\alpha_b = 2\times10^{-13}$ cm^3 s^{-1}, Q_{lyc} is the count rate of ionizing photons in s^{-1}, and R is the H II region radius.

An extremely compact H II region, e.g., one with $R < 100$ AU and corresponding density $n > 10^6$ cm^{-3}, would be optically thick and therefore fainter, $S_{95\mathrm{GHz}}(R = 100\mathrm{AU}, Q_{lyc} = 10^{47}\mathrm{s}^{-1}) = 3.4$ mJy. Even the brightest O-stars could produce H II regions as faint as 0.5 mJy if embedded in extremely high density gas; above $Q_{lyc} > 10^{47}$ s^{-1}, a 25 AU H II region would be ~ 0.5 mJy.

Figure 5 shows the predicted brightness for various H II regions produced by OB stars and the density required for those H II regions to be the specified size. In order for the detected sources to be O-star-driven H II regions, with $10^{47} < Q_{lyc} < 10^{50}$ s^{-1}, they must be optically thick and therefore extremely compact and dense. There is a narrow range of late O/early B stars, $10^{46} < Q_{lyc} < 10^{47}$ s^{-1}, that could be embedded in compact H II regions of almost any size and produce the observed range of flux densities. Anything fainter, later than ∼B0 ($Q_{lyc} < 10^{46}$ s^{-1}), would be incapable of producing the observed flux densities. Any brighter stars would have to be embedded in dust that, at 40 K, would outshine the H II region; more likely, such sources would have much hotter dust and therefore would be much brighter (and more extended) than our observations allow.

This restrictive parameter space, combined with a steep luminosity function that implies there are many more sources at slightly lower luminosity, is evidence against the population being dominated by H II regions. The spectral indices also support this conclusion.

4.1.4. *The sources are protostars*

After ruling out the other hypotheses, we conclude that these sources are predominantly embedded protostars. Their emission is likely dust-dominated, but is probably warmer than the cloud average $\sim 20-40$ K. We test and validate the hypothesis that most or all of the sources are protostellar in this section.

We cross-matched out source catalog with catalogs of H II regions and methanol masers. Class II methanol masers are always associated with sites of high-mass star formation. The Caswell et al. (2010) Methanol Multibeam Survey identified 11 sources in our observed field of view, of which 10 have a clear match in our catalog. Several other sources in our catalog match known H II regions from Gaume et al. (1995), mostly associated with the brightest sources in our sample; these all have $S_{3\mathrm{mm}} > 9$ mJy.

We compare our detected sample to that of the Herschel Orion Protostar Survey (HOPS; Furlan et al. 2016) in order to get a general sense of what types of sources we have detected. We selected this survey for comparison because it is one of the largest protostellar core samples with well-characterized bolometric luminosities available. Figure 6 shows the HOPS source fluxes at 870μm scaled to 3 mm assuming a dust opacity index $\beta = 1.5$, which is shallower than usually inferred, so the extrapolated fluxes may be slightly overestimated. The 870μm data were acquired with a $\sim 20''$ FWHM beam, which translates to a resolution $\sim 1''$ at $d_{SgrB2} = 8.4$ kpc assuming $d_{Orion} = 415$ pc, so our beam size is somewhat smaller than theirs. The HOPS sources are all fainter than the Sgr B2 sources. The brightest HOPS source, with $L_{tot} < 2000\ L_\odot$, would only be 0.2 mJy in Sgr B2, or about a 4-σ source - below our detection threshold even in the noise-free regions of the map. We conclude that the Sgr B2 sources are much more luminous and are therefore massive protostars.

This conclusion is supported by a more direct comparison with the Orion nebula as observed at 3 mm with MUSTANG (Dicker et al. 2009, Figure 7). Their data were taken at $9''$ FWHM resolution, corresponding to $0.48''$ at d_{SgrB2}. The peak flux density measured in that map is toward Source I, $S_{90GHz}(d_{SgrB2}) = 3.6$ mJy. Source I would therefore be detected and would be somewhere in the middle of our sample. It is extended, and the extended component would be readily detected in our data. Since Source I is the only known high-mass YSO in the Orion cloud, and it would be detectable while no other sources in the Orion cloud would be, it appears safe to conclude that all of our detected sources are MYSOs.

While we have concluded that the sources are dusty, massive protostars, the spectral indices we measured are somewhat surprising. Typical dust clouds in the Galactic disk have dust opacity indices $\beta \sim 1.5-2$ (Schnee et al. 2010; Shirley et al. 2011; Sadavoy et al. 2016). Our spectral indices are lower than these, with only 3 sources having measured $\beta = \alpha - 2 > 1.5$ (at the 2σ level, up to 11 sources are consistent with $\beta = 1.5$, but this is

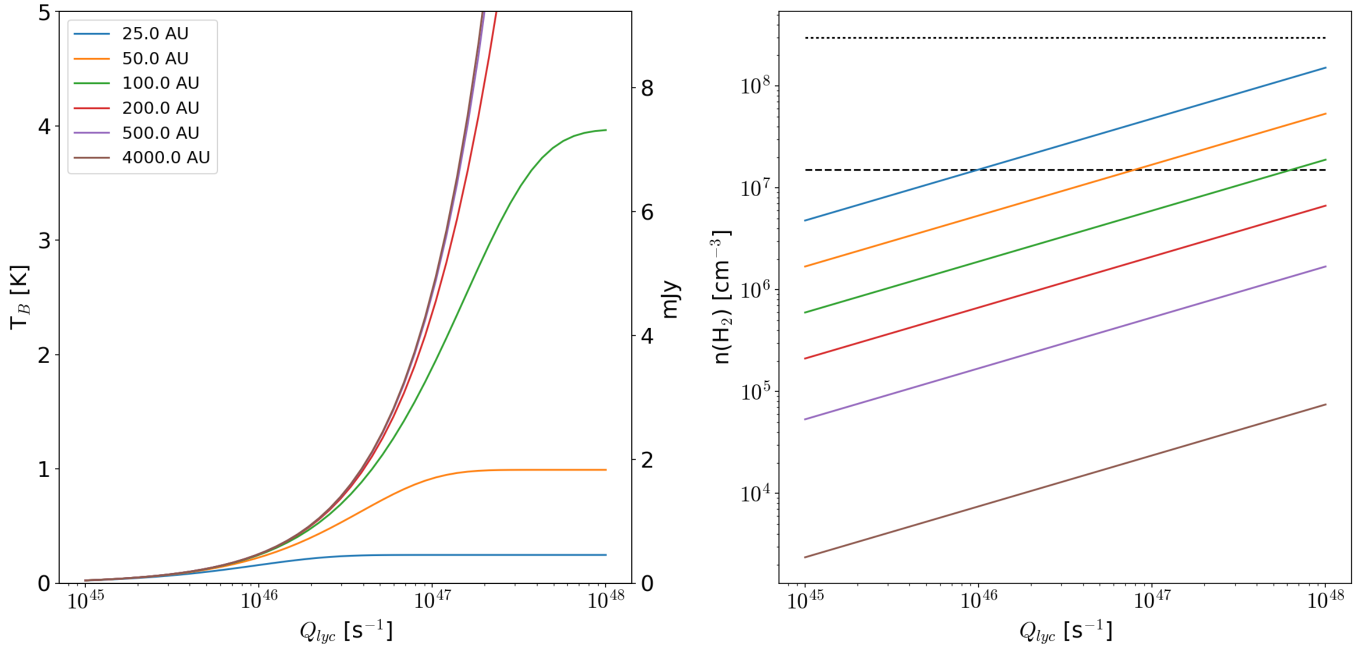

Figure 5. Simple models of spherical H II regions to illustrate the observable properties of such regions. The H II region size is shown by line color; the legend in the left plot applies to both figures. (left) The expected brightness temperature (left axis) and corresponding flux density within a FWHM=0.5″ beam (right axis) as a function of the Lyman continuum luminosity for a variety of source radii. (right) The density required to produce an H II region of that radius. The horizontal dashed line shows the density corresponding to an unresolved dust source at the 5-σ detection limit (≈ 0.5 mJy, or about 10 $M_\odot$ of dust, assuming $T = 40$ K). Above this line, dust emission would dominate over free-free emission. The dotted line shows the density required for dust emission to produce a 10 mJy source at $T = 40$ K. As seen in the left plot, for any moderate-sized H II region, $R > 100$ AU, a high-luminosity star ($Q_{lyc} > 10^{47}$ s^{-1}) would produce an H II region brighter than the majority of our sample, which includes only a few sources brighter than 10 mJy. The densities required to produce H II regions within our observed range ($1 < S_\nu < 10$ mJy) are fairly extreme, $n \gtrsim 10^6$ cm^{-3}, for O-stars.

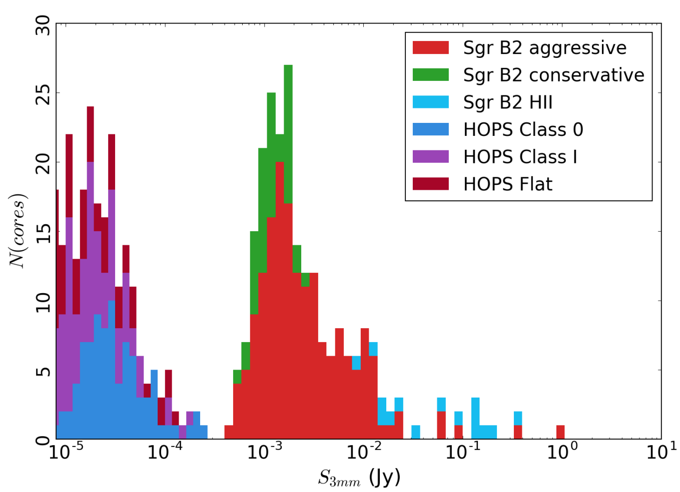

Figure 6. A histogram combining the detected Sgr B2 cores with predicted flux densities based on the HOPS (Furlan et al. 2016) survey. The HOPS histogram shows the 870 μm data from that survey scaled to 3 mm assuming $\beta = 1.5$. Every HOPS source is well below the detection threshold for our observations.

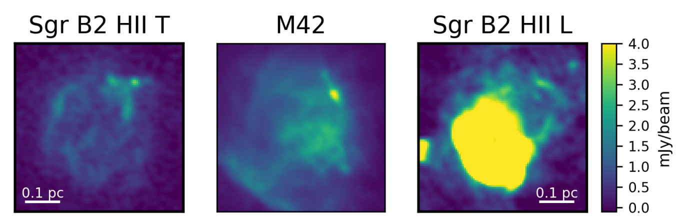

Figure 7. Comparison of two extended H II regions in Sgr B2 to the M42 nebula in Orion. The three panels are shown on the same physical and color scale assuming $d_{Orion} = 415$ pc and $d_{SgrB2} = 7.8$ kpc and that the ALMA and MUSTANG data have the same continuum bandpass. Sgr B2 H II T is comparable in brightness and extent to M42; Sgr B2 H II L is much brighter and is saturated on the displayed brightness scale. The compact source to the top right of the M42 image is Orion Source I; the images demonstrate that Source I and the entire M42 nebula would be easily detected in our data.

primarily because of their high measurement error). A shallower β implies free-free contamination, large dust grains, or optically thick surfaces are present within our sources. Since the above arguments suggest that the sources are high-mass protostars, the free-free contamination and optically thick inner region models are both plausible.

4.2. *Source distribution functions and the star formation rate*

The flux density distribution of the non-H II region sources follows a powerlaw with slope $\alpha = 1.94 \pm 0.07$ (fitted with the MLE method of Clauset et al. 2007). If we assume that the stellar mass is linearly proportional to the 3 mm continuum flux density, this measurement implies a slope shallower than the $\alpha \sim 2.35$ expected for a normal IMF. It is possible that the IMF is genuinely different from Salpeter here, but it is more likely that the more massive stars are surrounded by warmer gas, implying that the source mass distribution is steeper than the source flux distribution.

If we make the very simplistic assumptions that the sources we detect are all $L \gtrsim 2000\ L_\odot$ ($M \gtrsim 8 M_\odot$), we can infer the total (proto)stellar mass in the observed region. Using a Kroupa (2001) mass function with $M_{max} = 200\ M_\odot$, 23% of the mass is contained in $M > 8 M_\odot$ stars. Using $M = 8 M_\odot$ as the lower-limit case for each source, the identified sources have total mass $M(>8) = 1800 M_\odot$. The total stellar mass implied is $M_{tot} = 8 \times 10^3\ M_\odot$. If instead we assume each source has a mass equal to the mean stellar mass for $M > 8\ M_\odot$, $\bar{M} = 21.1\ M_\odot$, then the total inferred stellar mass is $M_{tot} = 2 \times 10^4\ M_\odot$. These are lower limits in the Sgr B2 N and M regions because our catalog is incomplete due to confusion and dynamic range limitations. Additionally, we are using a single-star IMF and our resolution is only ~ 4000 AU, so it is likely that we have undercounted by $\gtrsim 2\times$, since high-mass stars have a high multiplicity fraction (Mason et al. 2009).

For each subcluster, we count the number of H II regions identified in our survey plus those identified in previous works (de Pree et al. 1996) and we count the number of protostellar cores not associated with H II regions. To estimate the stellar mass, we assume each core contains a star with $M(8 \bar{-} 20) = 12\ M_\odot$ and each H II region contains a $\geq$B0 star with $M(\bar{>} 20) = 45\ M_\odot$. In Table 1, this estimate is shown as M_{obs}. We also compute the total stellar mass using the mass fractions $f(M > 20) = 0.14$ and $f(8 < M < 20) = 0.09$. The inferred masses computed from H II region counts and from core counts are shown in columns $M_{inferred,\mathrm{H\,II}}$ and $M_{inferred,cores}$ respectively; $M_{inferred}$ is the average of these two estimates. If our assumptions are correct and the mass distribution is governed by a power-law IMF, we expect $M_{inferred,\mathrm{H\,II}} = M_{inferred,cores}$. Except for Sgr B2 M, the core-based and H II-region based estimates agree to within $\sim 25\%$, which is about as good as expected from Poisson noise in the counting statistics. Sgr B2 M has the largest sample in both counts and has a factor of two discrepancy; this is likely because of the combined effects of source confusion at our $0.5''$ resolution and the increased noise around the extremely bright central region that makes detection of < 2 mJy sources impossible.

We compare our mass estimates to those of Schmiedeke et al. (2016), who inferred stellar masses primarily from H II region counts. The last two columns of Table 1 show the observed and estimated masses based on H II region counts. For Sgr B2 M and N, our results are similar, as expected since our catalogs are identical. For S and NE, we differ by a large factor: TODO: I don't know why; we have effectively the same source counts (though they have 1 more in South than I do) but significantly different inferred masses.

4.3. *An examination of star formation thresholds*

Many authors (e.g., Lada et al. 2010) have proposed that star formation can only occur above a certain density or column density threshold[1]. We discuss our measurements of column thresholds in this Section.

4.3.1. *Comparison to Lada, Lombardi, and Alves 2010*

In this section, we compare the star formation threshold in Sgr B2 to that in local clouds performed by Lada et al. (2010). They determined that all star formation in local clouds occurs above a column density threshold $M_{thresh} > 116\ M_\odot$ pc^{-2}, or $N_{thresh}(\mathrm{H}_2) > 5.2 \times 10^{21}$ cm^{-2} assuming the mean particle mass is 2.8 amu (Kauffmann et al. 2008). We first note, then, that *all pixels* in our column density maps are above this threshold by *at least* a factor of 10.

However, Sgr B2 is 8.5 kpc kpc away from us in the direction of our Galaxy's center, meaning there is a potentially enormous amount of material unassociated with the Sgr B2 cloud along the line of sight. This material may have column densities as low as $5{\times}10^{21}$ cm^{-2} or as high as $5{\times}10^{22}$ cm^{-2}, as measured from relatively blank regions in the Herschel column density map (Battersby et al. 2011). The former value corresponds to the background at high latitudes, $b \sim 0.5$, while the latter is approximately the lowest seen within our field of view. Even with the very aggressive foreground value of $5{\times}10^{22}$ cm^{-2} subtracted, nearly the whole Sgr B2 cloud exists above this threshold.

[1] Column density is more commonly used because of its observational convenience, but it is physically meaningless unless high column density leads to high optical depths and thereby changes the gas's ability to cool.

Table 1. Cluster Masses

Name	$N(cores)$	$N(H\text{II})$	M_{obs}	$M_{inferred}$	$M_{inferred,H\text{II}}$	$M_{inferred,cores}$	M^s_{obs}	M^s_{inf}
			$M_\odot$	$M_\odot$	$M_\odot$	$M_\odot$	$M_\odot$	$M_\odot$
M	15	52	2500	9500	17000	2000	1295	20700
N	10	7	440	1800	2300	1400	150	2400
NE	4	2	140	600	650	540	52	1200
S	3	1	81	370	330	410	50	1100
Total	216	73	5900	27000	24000	29000	1993	33400

To directly compare our observations to the star formation thresholds reported in Lada et al. (2010), we examined the column density associated with each millimeter continuum source. The Lada et al. (2010) data used a variable resolution for the column measurements toward their sample, ranging from 0.06-0.35 pc (equivalent to 1.5 to 9.2 $''$ at a distance of 8.5 kpc). The Herschel data we have available with per-pixel SED fits lack the resolution needed to make a direct comparison to the Lada et al data set, but the SHARC and SCUBA data have resolution approximately equivalent to that used in the Orion molecular cloud in their survey. We therefore use a range of temperatures bracketing the observed range in the Herschel maps ($\sim 20-50$ K) to produce column density maps from the SCUBA and SHARC data. Figure 8 shows the cumulative distribution function of the column density associated with each identified continuum source; the column density used is the nearest-neighbor pixel to the source in the column density maps. Even using the conservative maximum temperature $T_{dust} = 50$ K (resulting in the minimum column density), all of the sources exist at a column density an order of magnitude higher than the Lada threshold, and they exist above that threshold even if the foreground is assumed to be an extreme 5×10^{22} cm^{-2}.

The Lada et al. (2010) sample used Spitzer observations of nearby clouds that were nearly complete to stars at least as small as 0.5 $M_\odot$. By contrast, as discussed in Section 4.1.4, our survey is sensitive only to stars with $M \gtrsim 8\ M_\odot$. The apparently higher threshold either means that there is a genuinely higher threshold for star formation in the CMZ or that there is a higher threshold for high-mass star formation that may still be universal.

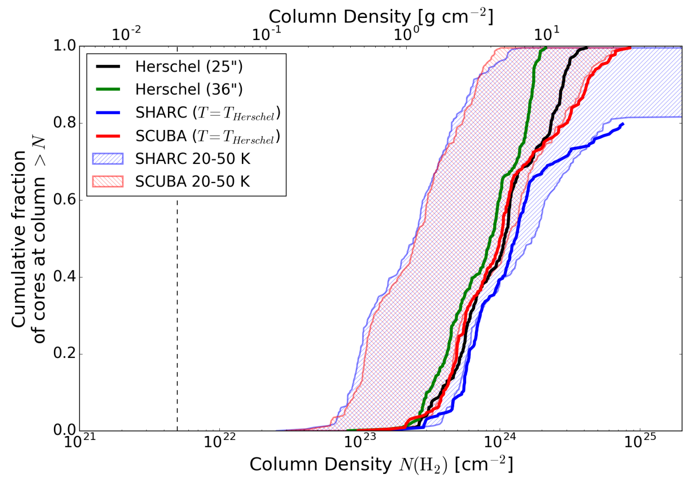

Figure 8. Cumulative distribution functions of the background column density associated with each identified 3 mm continuum source. The column densities are computed from a variety of maps with different resolution and assumed temperature. The Herschel maps use SED-fitted temperatures (Battersby et al. 2017) at 25 $''$ resolution (excluding the 500 μm data point) and 36 $''$ resolution. The SHARC 350 μm and SCUBA 450 μm maps both have higher resolution ($\sim 10''$) but no temperature information; we used an assumed $T_{dust} = 20$ and $T_{dust} = 50$ K to illustrate the range of possible background column densities (hatched red and blue). The thick solid red and blue lines show the SHARC and SCUBA column density images using Herschel temperatures interpolated onto their grids: these curves are closer to the 20 K than the 50 K curve and serve as the best estimate column density maps. The SHARC data fail to go to a cumulative fraction of 1 because the central pixels around Sgr B2 M and N are saturated (the lower temperature assumptions result in optical depths > 1, which cannot be converted to column densities using the optically thin assumption). The vertical dashed line shows the $N(\mathrm{H}_2) = 5.2 \times 10^{21}$ column density threshold from Lada et al. (2010).

4.3.2. *Comparison to other CMZ clouds*

In G0.253+0.016 (The Brick, G0.253), very little star formation has been observed (Longmore et al. 2013; Johnston et al. 2014; Rathborne et al. 2015) despite most of the cloud existing above the locally measured Lada et al. (2010) column density threshold. The column density distribution function for G0.253 is shown in Figure 10.

Comparing Sgr B2 to G0.253, the majority of the Sgr B2 cloud is at higher column than G0.253. The presence of star formation in Sgr B2 nearly all occurs at a higher column than exists within G0.253 (Figure 10). The lack

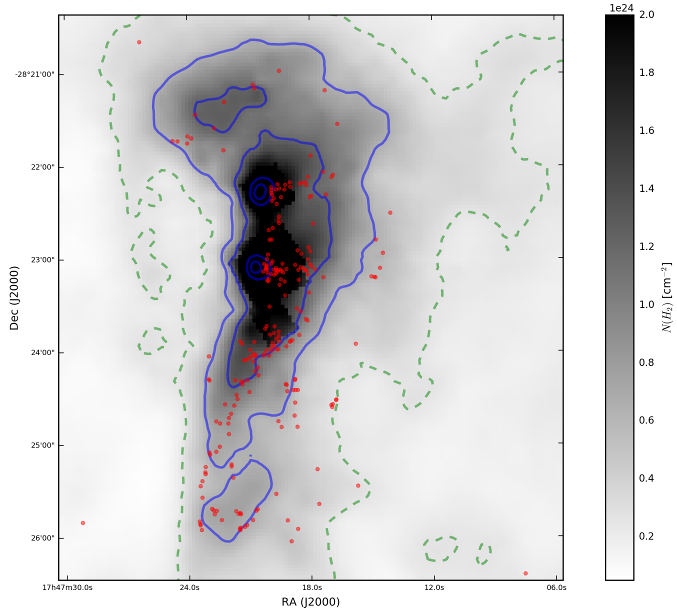

Figure 9. Overlay of the core locations on the SCUBA column density map created by interpolating the Herschel-measured temperatures onto the SCUBA grid and assuming the dust is optically thin at 450 μm. The square grid at the center shows a region affected by saturation in the Herschel data. Contours are shown at $N(\mathrm{H}_2) = 2 \times 10^{23}$ cm^{-2} (green dashed lines) and $N(\mathrm{H}_2) = 5, 10, 50, 100 \times 10^{23}$ cm^{-2} (blue lines). As shown in Figure 8, the threshold above which nearly all cores are found is high, but this figure shows that the core density is not well-correlated with the column density: there is a relative dearth of cores in the high-column north region and an overabundance in the moderate-column deep south region.

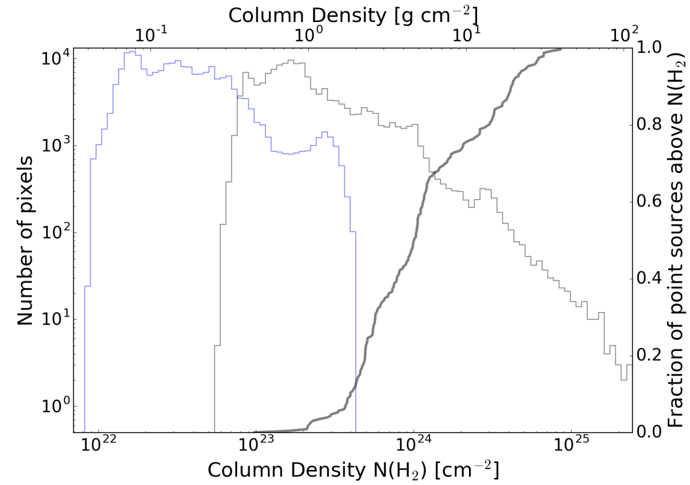

Figure 10. Histograms of the column density of G0.253+0.016 (blue) and Sgr B2 (gray) using the combined SCUBA 450 μm and Herschel 500 μm intensity with the interpolated Herschel dust temperatures. The cumulative distribution of core 'background' column densities in Sgr B2 is shown as a thick gray line.

of observed cores in The Brick is therefore consistent with the active SF seen in Sgr B2.

5. DISCUSSION

We have reported the detection of a large number of point sources and inferred that they are most likely all high-mass protostars. These sources universally reside in gas above $N \gtrsim 2 \times 10^{23}$ cm^{-2} gas. In this section, we discuss the implications of this apparent threshold for high-mass star formation in the CMZ.

A theoretical threshold for high-mass star formation, $N > 1$ g cm^{-2} was developed by Krumholz & McKee (2008). Since all of the sources we have detected reside above this threshold and we determined our sources are all likely to be massive protostars in Section 4.1.4, we have apparently confirmed this threshold.

While there is an apparent column density threshold required for high-mass stars to form, that threshold clearly forms only a necessary, not a sufficient, condition for star formation. Figure 11 shows that there is abundant material within our observed region at $N > 1$ g cm^{-2} that is not associated with ongoing high-mass star formation. These high-column-density, low star-formation regions are also evident in Figure 9, which shows that the northern and western regions of the cloud are the deficient zones.

5.1. *What drives star formation in the greater Sgr B2 complex?*

We have shown that, in addition to the known forming massive clusters, star formation is ongoing in an extended and elongated region to the north and south. Excluding the clusters, most of the newly discovered sources trace out long and linear features. Why are the sources aligned?

There is extended ionized emission in Sgr B2 Deep South that appears to be a bubble surrounded by the millimeter continuum sources. While this region looks like a normal, if a bit lumpy, H II region in the 12″ resolution 20 cm VLA data in Figure 3, the 3 mm continuum reveals long filamentary features reminiscent of the Galactic center arched filaments. By analogy, they may be magnetically dominated regions, but there must be some central source of ionizing radiation or energetic particles. Whatever the driver, it is possible that an expanding bubble of hot gas has compressed the molecular material along the ridge where we observe star formation.

By contrast, Sgr B2 Far North does not contain any ionized emission. It contains fewer total sources, but these sources trace the edge of an expanding bubble previously noted by de Vicente et al. (1997). The coinci-

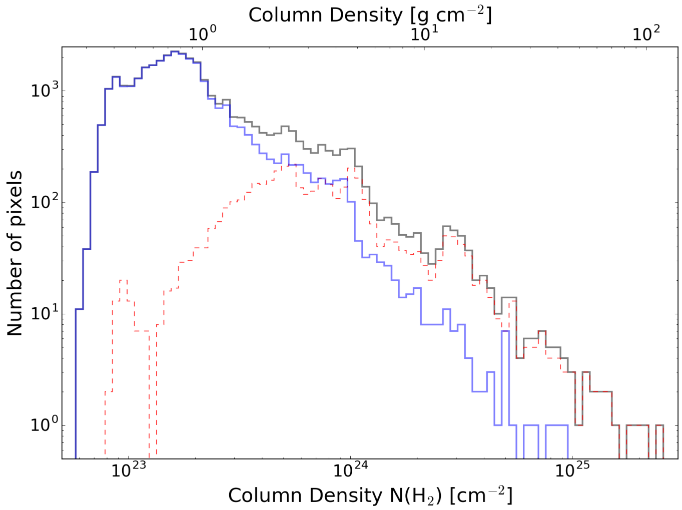

Figure 11. Histograms of the column density measured with the combined SCUBA and Herschel data using the interpolated Herschel temperatures covering only the region observed with ALMA. The black histogram shows the whole observed region, the blue solid shows the SCUBA pixels that do not contain an ALMA source, and the red dashed region shows those pixels that are within one beam FWHM of an ALMA source. While the ALMA sources (high mass protostars) clearly reside in high-column gas, there is abundant high-column material that shows no signs of ongoing star formation.

dence of star forming cores along the edge of a bubble again suggests some sort of compressional triggering.

However, while both of these regions show circumstantial, morphological evidence for a compressional event, there are other regions within our map that show the same general morphology in the gas, yet exhibit no star formation.

The morphological features can be seen in Figure 12. The molecular gas, as traced by HC_3N in this case, outlines bubble edges in all directions from Sgr B2 M. The eastern edge shows the clearest bubble in this image, with the HC_3N outlining a cavity in the column density map. The edge of this eastern bubble has a lower average column density than either the northern Sgr B2 NE or the Sgr B2 DS regions, and it shows no signs of ongoing star formation. By contrast, the bubble edges in the Sgr B2 NE and the ridge Sgr B2 W both contain some protostars, and the Sgr B2 DS ridge has the most.

6. CONCLUSIONS

We have reported the detection of 237 3 mm point sources in the extended Sgr B2 cloud, and determined that the majority are high-mass protostellar cores. This survey represents the first large population of protostars detected in the Galactic center and represents the largest sample yet reported of high-mass protostars.

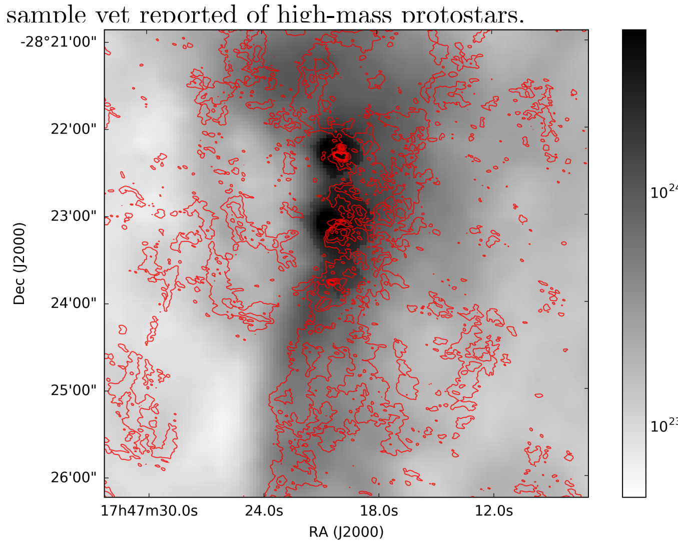

Figure 12. ALMA HC_3N peak intensity contours (orange) overlaid on the derived SCUBA column density image using Herschel Hi-Gal interpolated temperatures. The HC_3N was shown in grayscale in Figure 4. Contours are at levels [3,7,11,15,19,23] K. The HC_3N bubble edges can be seen surrounding cavities in the SCUBA column density map on the east side of the main ridge. To the north, the HC_3N also traces bubbles, but these are less evident in this velocity-integrated view. The important feature discussed in Section 5.1 is the differing column density around each of the bubbles.

Software: The software used to make this version of the paper is available from github at `https://github.com/keflavich/W51_ALMA_2013.1.00308.S` with hash d4509bb (2017-05-18).

REFERENCES

Bally, J., Aguirre, J., Battersby, C., et al. 2010, ApJ, 721, 137

Barnes, A. T., Longmore, S., Battersby, C., Bally, J., & Kruijssen, J. M. D. 2016, arXiv:1609.08478v1

Barnes, A. T., Longmore, S. N., Battersby, C., et al. 2017, ArXiv e-prints, arXiv:1704.03572

Battersby, C., Bally, J., & Svoboda, B. 2017, ApJ, 835, 263

Battersby, C., Bally, J., Ginsburg, A., et al. 2011, A&A, 535, A128

Caswell, J. L., Fuller, G. A., Green, J. A., et al. 2010, MNRAS, 404, 1029

Chapin, E. L., Berry, D. S., Gibb, A. G., et al. 2013, MNRAS, 430, 2545

Clauset, A., Rohilla Shalizi, C., & Newman, M. E. J. 2007, ArXiv e-prints, arXiv:0706.1062

Condon, J. J., & Ransom, S. 2007, Essential Radio Astronomy (NRAO). http://www.cv.nrao.edu/course/astr534/ERA.shtml

de Pree, C. G., Gaume, R. A., Goss, W. M., & Claussen, M. J. 1996, ApJ, 464, 788

de Vicente, P., Martin-Pintado, J., & Wilson, T. L. 1997, A&A, 320, 957

Di Francesco, J., Johnstone, D., Kirk, H., MacKenzie, T., & Ledwosinska, E. 2008, ApJS, 175, 277

Dicker, S. R., Mason, B. S., Korngut, P. M., et al. 2009, ApJ, 705, 226

Dowell, C. D., Lis, D. C., Serabyn, E., et al. 1999, in Astronomical Society of the Pacific Conference Series, Vol. 186, The Central Parsecs of the Galaxy, ed. H. Falcke, A. Cotera, W. J. Duschl, F. Melia, & M. J. Rieke, 453

Furlan, E., Fischer, W. J., Ali, B., et al. 2016, ApJS, 224, 5

Gaume, R. A., Claussen, M. J., de Pree, C. G., Goss, W. M., & Mehringer, D. M. 1995, ApJ, 449, 663

Ginsburg, A., Glenn, J., Rosolowsky, E., et al. 2013, ApJS, 208, 14

Ginsburg, A., Walsh, A., Henkel, C., et al. 2015, A&A, 584, L7

Ginsburg, A., Henkel, C., Ao, Y., et al. 2016, A&A, 586, A50

Henshaw, J. D., Longmore, S. N., Kruijssen, J. M. D., et al. 2016, MNRAS, 457, 2675

Immer, K., Kauffmann, J., Pillai, T., Ginsburg, A., & Menten, K. M. 2016, A&A, 595, A94

Johnston, K. G., Beuther, H., Linz, H., et al. 2014, A&A, 568, A56

Kauffmann, J., Bertoldi, F., Bourke, T. L., Evans, II, N. J., & Lee, C. W. 2008, A&A, 487, 993

Kauffmann, J., Pillai, T., Zhang, Q., et al. 2016a, ArXiv e-prints, arXiv:1610.03499

—. 2016b, ArXiv e-prints, arXiv:1610.03502

Kroupa, P. 2001, MNRAS, 322, 231

Krumholz, M. R., & McKee, C. F. 2008, Nature, 451, 1082

Lada, C. J., Lombardi, M., & Alves, J. F. 2010, ApJ, 724, 687

Longmore, S. N., Kruijssen, J. M. D., Bally, J., et al. 2013, MNRAS, 433, L15

Mason, B. D., Hartkopf, W. I., Gies, D. R., Henry, T. J., & Helsel, J. W. 2009, AJ, 137, 3358

Mehringer, D. M., de Pree, C. G., Gaume, R. A., Goss, W. M., & Claussen, M. J. 1995, ApJL, 442, L29

Molinari, S., Swinyard, B., Bally, J., et al. 2010, A&A, 518, L100

Molinari, S., Schisano, E., Elia, D., et al. 2016, A&A, 591, A149

Ossenkopf, V., & Henning, T. 1994, A&A, 291, 943

Ossenkopf-Okada, V., Csengeri, T., Schneider, N., Federrath, C., & Klessen, R. S. 2016, A&A, 590, A104

Pierce-Price, D., Richer, J. S., Greaves, J. S., et al. 2000, ApJL, 545, L121

Pree, C. G. D., Peters, T., Low, M. M. M., et al. 2015, arXiv:1511.05131v1

Rathborne, J. M., Longmore, S. N., Jackson, J. M., et al. 2015, ApJ, 802, 125

Sadavoy, S. I., Stutz, A., Schnee, S., et al. 2016, arXiv:1601.06769v1

Sahai, R., Güsten, R., & Morris, M. R. 2012a, ApJL, 761, L21

Sahai, R., Morris, M. R., & Claussen, M. J. 2012b, ApJ, 751, 69

Sanchez-Monge, A., Schilke, P., Schmiedeke, A., et al. 2017, ArXiv e-prints, arXiv:1704.01805

Schmiedeke, A., Schilke, P., Möller, T., et al. 2016, A&A, 588, A143

Schnee, S., Enoch, M., Noriega-Crespo, A., et al. 2010, ApJ, 708, 127

Shetty, R., Beaumont, C. N., Burton, M. G., Kelly, B. C., & Klessen, R. S. 2012, MNRAS, 425, 720

Shirley, Y. L., Mason, B. S., Mangum, J. G., et al. 2011, AJ, 141, 39

Stanimirovic, S. 2002, in Astronomical Society of the Pacific Conference Series, Vol. 278, Single-Dish Radio Astronomy: Techniques and Applications, ed. S. Stanimirovic, D. Altschuler, P. Goldsmith, & C. Salter, 375–396

Yusef-Zadeh, F., Hewitt, J. W., & Cotton, W. 2004, ApJS, 155, 421

APPENDIX

A. SINGLE DISH COMBINATION

To measure the column density at a resolution similar to Lada et al. (2010), we needed to use ground-based single-dish data with resolution $\sim 10''$. We combined these images with Herschel data, which recover all angular scales, to fill in the missing 'short spacings' from the ground-based data.

Specifically, we combine the SHARC 350 μm (Dowell et al. 1999) and SCUBA 450 μm (Pierce-Price et al. 2000; Di Francesco et al. 2008) with Herschel 350 and 500 μm data (Molinari et al. 2016), respectively.

Combining single-dish with 'interferometer' data, or data that are otherwise insensitive to large angular scales, is not a trivial process. The standard approach advocated by the ALMA project is to use the 'feather' process, in which two images are fourier-transformed, multiplied by a weighting function, added together, and fourier transformed back to image space (see equations in §5.2 of Stanimirovic 2002). This process is subject to substantial uncertainties, particularly in the choice of the weighting function.

Two factors need to be specified for linear combination: the beam size of the 'single-dish', or total power, image, and the largest angular scale of the 'interferometer' or filtered image. While the beam size is sometimes well-known, for single dishes operating at the top of their usable frequency range (e.g., the CSO at 350 μm or GBT at 3 mm), there are uncertainties in the beam shape and area and there are often substantial sidelobes. In interferometric data, the largest angular scale is well-defined in the originally sampled UV data, but is less well-defined in the final image because different weighting factors change the recovered largest angular scale. For ground-based filtered data, the largest recoverable angular scale is difficult to determine and requires concerted effort (e.g., Ginsburg et al. 2013; Chapin et al. 2013).

To assess the uncertainties in image combination, particularly on the brightness distribution (e.g. Ossenkopf-Okada et al. 2016), we have performed a series of experiments combining the Herschel with the SCUBA data using different weights applied to the SCUBA data. As discussed in Section 2, we empirically determined the scale factor required for the best match between SCUBA and Herschel data was 3×, which is shockingly large but justifiable. In the experiment shown in Figure 13, we show the images and resulting histograms when we combine the Herschel data with the SCUBA data scaled by a range of factors from 0.5× to 10×. The changes to the high end of the histogram are dramatic, but the middle region containing most of the pixels (and most relevant to the discussion of thresholds in the paper) is hardly affected. Additionally, we show the cumulative distribution function of core background surface brightnesses (as in Figure 8), showing again that only the high end is affected.

B. SELF-CALIBRATION

We demonstrate the impact of self-calibration in this section. The adopted approach used three iterations of phase-only self-calibration followed by two iterations of phase and amplitude self-calibration. Each iteration involved slightly different imaging parameters. The final, deepest clean used a threshold mask on the previous shallower clean. The script used to produce the final images is available at `https://github.com/keflavich/SgrB2_ALMA_3mm_Mosaic/blob/d4509bb\protect\let\futurelet\@let@token\let\let\relax/script_merge/selfcal_continuum_merge_7m.py`. The effects are shown with a cutout centered on the most affected region around Sgr B2 M in Figure 14.

C. PHOTOMETRIC CATALOG

We include the full catalog here.

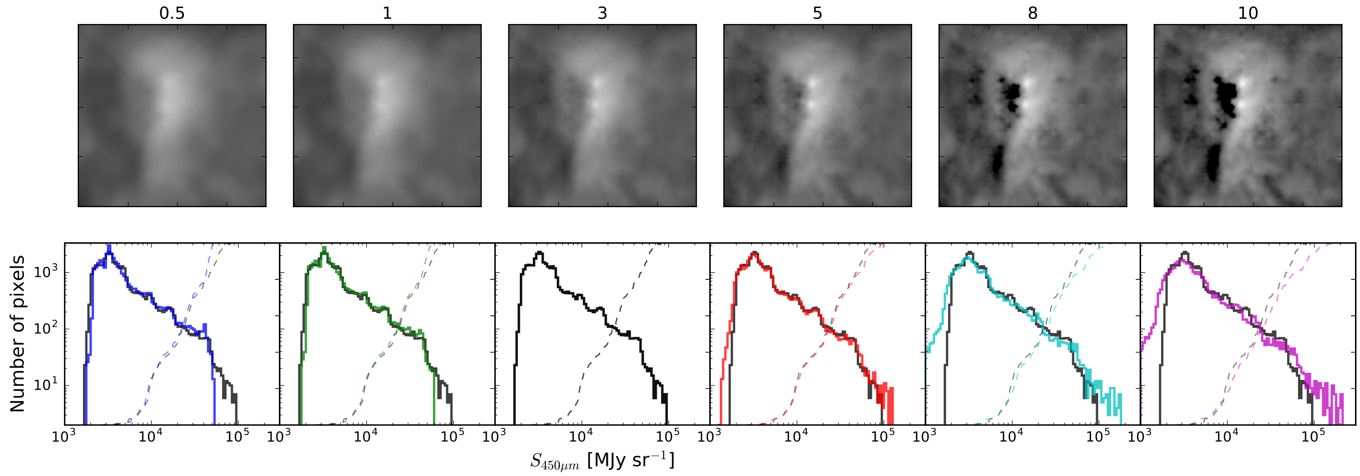

Figure 13. A demonstration of the effects of using different calibration factors when combining the SCUBA data with the Herschel data using the 'feather' process. The numbers above each panel show the scale factor applied to the SCUBA data before fourier-combining it with the Herschel data. The factor of 3 was used in this paper and shows the most reasonable balance between the high-resolution of the SCUBA data and the all-positive Herschel data. In the lower panels, the fiducial scale factor of 3 is shown in black in all panels. The solid lines show histograms of the images displayed in the top panels. The dashed lines show the cumulative distribution of the background surface brightnesses of the point sources in this sample; they are similar to the distributions shown in Figure 8.

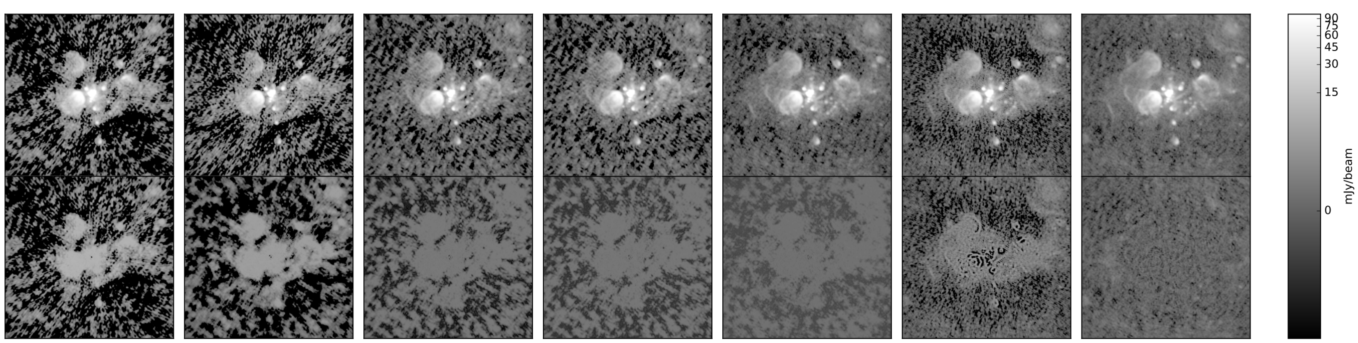

Figure 14. Progression of the self-calibration iterations. The images show, from left to right, the initial image, one, two, and three iterations of phase-only self calibration, one iteration of phase and amplitude self-calibration, one iteration of phase and amplitude self-calibration using two Taylor terms and multiscale clean for the imaging, and finally, a reimaging of the last iteration with a deeper 0.1 mJy threshold using a mask at the 2.5 mJy level. The second row shows the corresponding residual images.

Table 2. Continuum Source IDs and photometry

ID	Coordinates	$S_{nu,max}$	$T_{B,max}$	$S_{nu,tot}$	σ_{bg}	α	$E[\alpha]$	$M(20K)$	$N(\mathrm{H}_2, 20K)$	Classification
		mJy beam^{-1}	K	mJy	mJy beam^{-1}			$\mathrm{M}_\odot$	cm^{-2}	
47	17:47:17.703 -28:25:16.05	0.47	0.25	17	0.04	7.5	11	17	1.6×10^{24}	S
121	17:47:22.463 -28:24:46.23	0.49	0.25	1.9	0.08	3.2	4.5	17	1.7×10^{24}	S
120	17:47:22.654 -28:24:44.89	0.51	0.27	22	0.06	4.5	6.4	18	1.7×10^{24}	S
10	17:47:23.36 -28:25:34.25	0.52	0.27	11	0.04	-0.73	1	18	1.8×10^{24}	S
207	17:47:22.67 -28:25:04.6	0.55	0.29	23	0.04	4.8	6.8	2	1.9×10^{24}	W
119	17:47:15.72 -28:25:26.84	0.58	0.3	23	0.04	3.5	5	21	2×10^{24}	S
213	17:47:18.991 -28:26:02.695	0.61	0.32	27	0.08	2.4	3.4	22	2.1×10^{24}	W
54	17:47:20.871 -28:25:48.75	0.62	0.33	27	0.04	1.8	2.6	22	2.1×10^{24}	S
142	17:47:19.617 -28:24:44.88	0.62	0.33	29	0.05	2.1	3	22	2.1×10^{24}	S
206	17:47:18.675 -28:24:48.596	0.63	0.33	24	0.04	3.7	5.3	22	2.1×10^{24}	W
158	17:47:21.507 -28:25:55.22	0.65	0.34	24	0.05	8.5	12	23	2.2×10^{24}	S
45	17:47:22.487 -28:25:01.37	0.7	0.37	2	0.03	2.2	3.1	25	2.4×10^{24}	S
60	17:47:17.268 -28:21:10.96	0.71	0.37	28	0.06	5.4	7.7	25	2.4×10^{24}	S
210	17:47:22.751 -28:25:44.861	0.73	0.38	37	0.16	3.6	5	26	2.5×10^{24}	W
203	17:47:17.012 -28:24:34.624	0.76	0.4	37	0.07	3.4	4.9	27	2.6×10^{24}	W
211	17:47:21.47 -28:25:45.039	0.76	0.4	34	0.18	0.32	0.46	27	2.6×10^{24}	W
160	17:47:22.646 -28:25:42.794	0.76	0.4	3	0.11	-0.69	0.97	27	2.6×10^{24}	S
62	17:47:14.069 -28:22:30.51	0.76	0.4	29	0.04	0.41	0.58	27	2.6×10^{24}	S
50	17:47:21.526 -28:25:54.33	0.77	0.4	27	0.06	1.7	2.3	27	2.6×10^{24}	S
212	17:47:21.165 -28:25:51.985	0.79	0.42	35	0.07	1.5	2.2	28	2.7×10^{24}	W
49	17:47:21.487 -28:25:53.72	0.8	0.42	38	0.05	1.4	2	29	2.7×10^{24}	S
21	17:47:22.036 -28:24:53.23	0.8	0.42	31	0.04	5.4	7.6	29	2.8×10^{24}	S
205	17:47:19.448 -28:24:48.815	0.81	0.43	45	0.07	0.46	0.65	29	2.8×10^{24}	W
146	17:47:19.177 -28:24:25.49	0.82	0.43	38	0.08	0.35	0.5	29	2.8×10^{24}	S
61	17:47:16.648 -28:21:32.74	0.83	0.44	29	0.04	-1.1	1.6	3	2.8×10^{24}	S
199	17:47:22.982 -28:24:18.367	0.84	0.44	37	0.11	4	5.6	3	2.9×10^{24}	W
51	17:47:22.414 -28:25:48.82	0.84	0.44	43	0.06	4.8	6.8	3	2.9×10^{24}	S
64	17:47:14.795 -28:22:47.82	0.86	0.45	34	0.09	4.7	6.6	31	3×10^{24}	S
48	17:47:19.736 -28:25:32.03	0.88	0.46	39	0.05	6.5	9.3	31	3×10^{24}	S
217	17:47:17.373 -28:23:11.991	0.88	0.46	38	0.1	6.2	8.8	31	3×10^{24}	W
223	17:47:23.99 -28:21:40.491	0.89	0.47	36	0.05	1.2	1.6	32	3×10^{24}	W
218	17:47:19.27 -28:23:14.742	0.9	0.47	33	0.14	-1.6	2.2	32	3.1×10^{24}	W
8	17:47:23.357 -28:25:23.58	0.91	0.48	37	0.06	5.7	8	32	3.1×10^{24}	S
196	17:47:21.718 -28:24:18.354	0.91	0.48	41	0.22	7.9	11	33	3.1×10^{24}	W
200	17:47:23.024 -28:24:17.719	0.92	0.48	49	0.23	3	4.2	33	3.1×10^{24}	W